

Chapter 2

Towards an Integrative Inversion and Interpretation of Airborne and Terrestrial Data

Hans-Jürgen Götze, Martin Afanasjew, Michael Alvers, Liliana Barrio-Alvers, Ralph-Uwe Börner, Christian Brandes, Rudolf Eröss, Peter Menzel, Uwe Meyer, Mathias Scheunert, Bernhard Siemon, Klaus Spitzer, Dominik Steinmetz, Johannes Stoll, Gupta Sudha, Bülent Tezkan, Angelika Ullmann and Jutta Winsemann

Abstract The aim of the joint research project is to generate information from airborne geophysical measurements that are properly transferred from physically quantitative descriptions of the subsurface (electrical conductivities, densities, susceptibilities) into spatial structures and information matching the understanding of end-users: geologists, hydrogeologists, engineers and others. We suggest new types of inversion, which are integrated in the interactive workflow to support typical trial and error approaches of inverse and forward EM and gravity/magnetic field modelling for 1D and 3D cases. Subsequently, we combine resistivity and density models with geological 3D subsurface models. The integrated workflow minimizes uncertainties

H.-J. Götze (✉) · P. Menzel

Institut für Geowissenschaften, Christian-Albrechts-Universität Kiel, Kiel, Germany
e-mail: hajo@geophysik.uni-kiel.de

U. Meyer · B. Siemon · A. Ullmann

Abteilung Grundwasser und Boden, Bundesanstalt für Geowissenschaften und Rohstoffe, Hannover, Germany

R. Eröss · G. Sudha · B. Tezkan

Institut für Geophysik und Meteorologie, Universität zu Köln, Cologne, Germany

J. Stoll

Mobile Geophysical Technologies, Celle, Germany

R.-U. Börner · M. Scheunert · K. Spitzer

Institut für Geophysik und Geoinformatik, TU Bergakademie Freiberg, Freiberg, Germany

M. Afanasjew

Institut für Numerische Mathematik und Optimierung, TU Bergakademie Freiberg, Freiberg, Germany

M. Alvers

Transinsight GmbH Dresden, Dresden, Germany

C. Brandes · D. Steinmetz · J. Winsemann

Institut für Geologie, Leibniz Universität Hannover, Hannover, Germany

L. Barrio-Alvers

Biotechnologie Zentrum, Technische Universität Dresden, Dresden, Germany

in the interpretation of geophysical data and allows a significantly improved and fast interpretation and imaging of the 3D subsurface architecture. The results of the AIDA project demonstrate that combined 3D geological and geophysical models enable a much better reconstruction of the subterranean space. AIDA stands for “From Airborne Data Inversion to In-Depth Analysis” and is part of the R&D program: Tomography of the Earth’s Crust—From Geophysical Sounding to Real-Time Monitoring.

2.1 Introduction

The rising competition in land use especially between water economy, agriculture, forestry, building material economy and other industries often lead to irreversible deterioration in the water and soil system (e.g. salinization and degradation) due to over-exploitation which results in a long term damage of natural resources. Spatial surveys of the subsurface structure and physical parameters by airborne geophysical measurements and subsequent ground geophysical surveys target exemplarily at two test sites (Cuxhaven and Rhüden, Fig. 2.1) enabling to gain the needed additional knowledge. The complementary use of airborne and ground geophysics, the validation, assimilation and improvement of current results by inversion techniques and plausibility tests helped us to respond to the following key questions: (1) Which algorithms are useful to describe structural settings of the usable subsurface by user specific characteristics as e.g. water volume, layer thicknesses, porosities. (2) What are the physical relations of observed parameters (electrical conductivities, magnetic susceptibilities, densities, etc.) to geological strata? (3) How can we deduce characteristics or parameters from the observations which describe near subsurface structures (e.g. groundwater systems, their charge, discharge and recharge, vulnerabilities and other quantities)?

The six partners of the AIDA project (AIDA: From Airborne Data Inversion to In-Depth Analysis) developed new and expanded existing inversion strategies to improve structural parameter information on different space and time scales and tested them for a multi-parameter inversion applying interactive graphic tools. A primary goal was also to solve comparable society related problems (as salinization, erosion, contamination, degradation etc.) in regions within Germany by generalization of project results. Modelling results from the different projects are still based on very heterogeneous modelling software and philosophies. We harmonized results for comparison, validation and synoptic visualization (Sect. 2.7). Validation and definition of geological units were based on 3D-subsurface models of electrical resistivity, borehole logs, gravity/magnetics and seismic models as constraints. A GOCAD[®] model of the tunnel valley is used as constrain for geophysical-modelling in appropriate software.

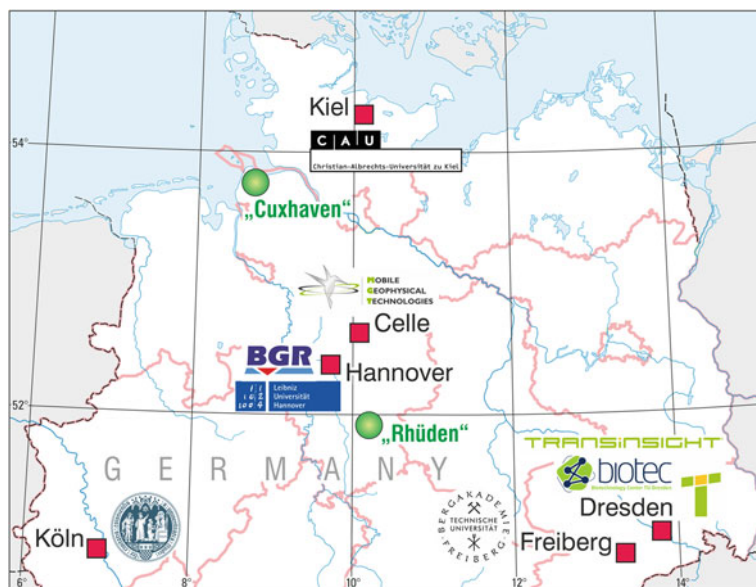


Fig. 2.1 Location map of AIDA partners and their research areas: the Cuxhaven subglacial tunnel valley in the North and the Lutter anticline near Rhüden in the center

2.2 Data Bases

We selected three areas to test our recently developed algorithms and the work flow. Two areas are located in the Central European Basin System (CEBS). The basin developed in the Permian as a rift basin (Littke et al. 2008). The up to 10 km thick basin fill comprises Lower Permian to Neogene continental and marine deposits. During the Pleistocene the CEBS was affected by repeated glaciations and transgressed by the Scandinavian ice sheets. Two test sites were chosen, the Cuxhaven subglacial tunnel valley and its Neogene host sediments and a salt anticline (Lutter anticline) in the northwestern part of the Harz foreland plus a third location in Switzerland.

Cuxhaven tunnel valley

The Cuxhaven tunnel valley is located in northwestern Germany, between Cuxhaven and Bremerhaven (Fig. 2.1). This area is characterized by the occurrence of numerous Middle Pleistocene subglacial tunnel valleys, which are deeply incised into Neogene and Palaeogene marginal marine deposits. These tunnel valleys are often important groundwater reservoirs and have a complex fill, reflecting repeated cut-and fill processes. The Cuxhaven tunnel valley is about 350 m deep and 1–2 km wide. The lower fill consists of interbedded gravel, sand and silt, deposited by meltwater. In the upper part fine-grained glacio-lacustrine deposits (Lauenburg clay complex) and interglacial marine Holsteinian deposits occur. During the subsequent Saalian glaciation an up to 40 m thick terminal moraine formed that consists

of meltwater deposits and till, flanked by younger Eemian and Holocene intertidal and salt marsh sediments. The data base includes airborne electromagnetics (AEM), comprising both frequency-domain helicopter-borne electromagnetic data (HEM) and time-domain helicopter-borne electromagnetic data (SkyTEM), helicopter-borne magnetic (HMG) and radiometric (HRD) measurements, ground-based continuous vertical electrical soundings (CVES), time-domain electromagnetics (TEM), direct current (DC), 2D reflection seismic profiles, gravimetric data sets and borehole logs were made available.

Lutter anticline (Rhüden)

The Lutter anticline lies within the Harz foreland area, 10 km northeast of Rhüden (Fig. 2.1). It represents a salt-cored anticline that formed during the Cretaceous contraction phase of the CEBS. The broad anticline trends NNE-SSW, is approximately 5 km wide and composed of Mesozoic sedimentary rocks. The data base includes an airborne survey comprising HEM, HMG and HRD and ground based gravity data.

Neuchâtel (Swiss)

The suitability of the test area (an electric cable and a pipeline) was proven by preceding geophysical investigations performed by subproject 1. It was chosen due to the vicinity to Luzern, where *Aeroscout* has its office and strong known anomalies occur. The VLF-method is sensitive for lateral conductivity changes. The prominent anomalies ensured a strong signal, this way, despite all kind of different noise and problems that may occur in a pilot project area, we ensured that the first UAS-VLF survey was able to resolve the anomalies.

2.3 Aero-Ground Inversion

One of the central project objectives was the combination of an unmanned aerial system (UAS) with the very low frequency (VLF) method. It will help to bridge the gap between conventional aero- and terrestrial geophysics. An UAS is capable of navigating precisely and is therefore suited for geophysical measurements flying with low and constant velocity at low altitudes across areas of interest. The strength of the VLF method is the ability to quickly map areas. In March 2012 a first experiment UAS-VLF measurements were conducted with a prototype system on a test area close to Neuchâtel in Switzerland (N 47.025, E 7.016). This system consists of a three-component electromagnetic sensor and a data logger deployed on an unmanned helicopter (Fig. 2.2). To receive comparable data ground based VLF and UAS-VLF measurements were carried out. Time series of the H_x , H_y and H_z components were processed to derive the transfer functions. The measurements of both methods clearly indicate the location of the anomalies. A data example of the survey is shown in Fig. 2.3. The relation of the horizontal and vertical magnetic field components $H_z(f) = A(f) \cdot H_x(f) + B(f) \cdot H_y(f)$ is used to derive the magnetic transfer function $A(f) = H_z(f) \cdot H_x(f)$.

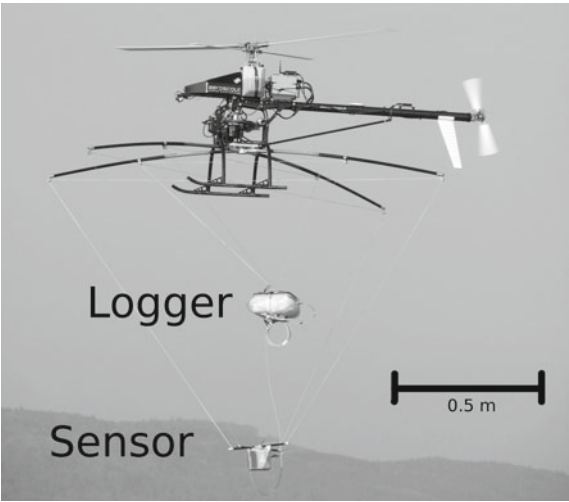


Fig. 2.2 The UAS-VLF-system with the logger and sensor hanging on the suspension. The especially developed suspension satisfies numerous functions. It mitigates oscillations, rotations and vibrations of the sensor and the logger and, additionally, helps to reduce torques caused by the devices (onto the helicopter). A reasonable compromise between low noise and flight stability had to be found. Additionally, the logger and the sensor went through a weight reduction process

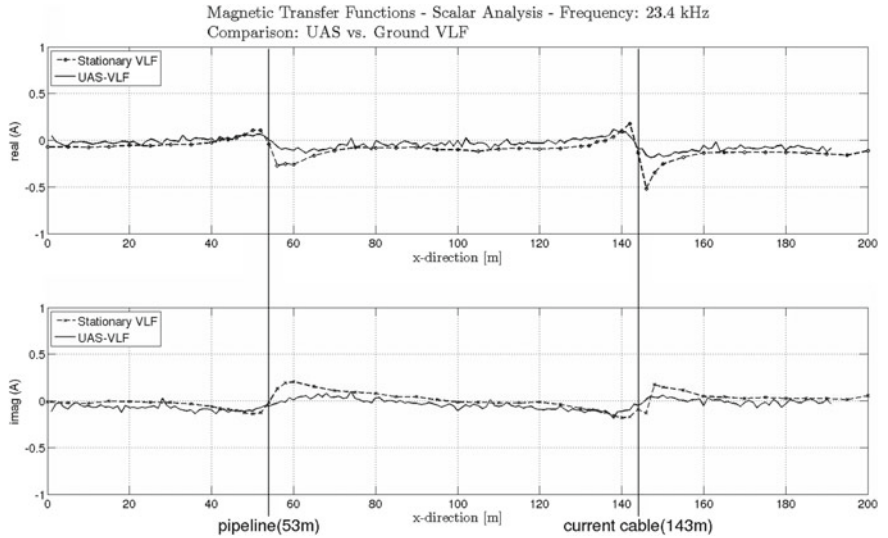


Fig. 2.3 Scalar analysis and comparison of the stationary ground and UAS-VLF measurements of the A component of the magnetic transfer function along a common transect. The real (*top*) and imaginary part (*bottom*) of the magnetic transfer functions is shown along the profile distance in meters. The 23.4 kHz frequency is utilized

As expected, the amplitudes of the ground based VLF measurements are bigger and the transfer function is less noisy compared to the UAS-VLF measurements. Nevertheless, the anomalies (inflection points) are clearly visible for both methods and the their locations could successfully be detected by the UAS-VLF and ground based VLF measurements. The time series were analyzed by the scalar as well bivariate methods. For more details see Eröss et al. (2013).

The accuracy of model parameters for inversion was improved at shallow and greater depths. HEM, TEM and RMT measurements have been combined by using a 1D joint inversion methodology. To obtain this, the data sets, the model functions and the Jacobian matrices of these methods are combined to acquire only one set of model parameters as described below.

$$\mathbf{d} = \begin{pmatrix} \mathbf{d}_1(RMT) \\ \mathbf{d}_2(HEM) \\ \mathbf{d}_3(TEM) \end{pmatrix}, \mathbf{J} = \begin{pmatrix} \mathbf{J}_1(RMT) \\ \mathbf{J}_2(HEM) \\ \mathbf{J}_3(TEM) \end{pmatrix}, \mathbf{f} = \begin{pmatrix} \mathbf{f}_1(RMT) \\ \mathbf{f}_2(HEM) \\ \mathbf{f}_3(TEM) \end{pmatrix}, \quad (2.1)$$

where \mathbf{d} is the measured data vector and \mathbf{f} is the computed response that correspond to the logarithms of in-phase and quadrature components, induced voltages, and apparent resistivities and phases for HEM, TEM and RMT data, respectively. \mathbf{J} is the Jacobian matrix containing the parameter sensitivities, i.e. the derivatives of the functional \mathbf{f} with respect to the model parameters \mathbf{m} . The objective of the joint inversion of three different electromagnetic methods is to explore the Earths subsurface from shallow to deep structures. This has led us to construct a matrix whose elements are based on the selected method and corresponding model parameter. The newly developed algorithm functions as follows:

1. Choose maximum and minimum value of depth of investigations, for all the methods used, following Spies (1989). Out of these, four depths of investigation indices will be used, which are $d_{max}(RMT)$, $d_{min}(HEM)$, $d_{max}(HEM)$ and $d_{min}(TEM)$. Where $d_{max}(RMT)$ is the maximum depth down to which RMT can resolve well. Consequently, $d_{min}(HEM)$ and $d_{max}(HEM)$ are the minimum and maximum depths which HEM can resolve well. Similarly, $d_{min}(TEM)$ is the minimum depth above which TEM cannot resolve earth structures sufficiently.
2. Choose a starting model.
3. Derive model parameter weighting matrix \mathbf{W}_m : If $d_i \geq d_{max}(RMT)$; elements of the weighting matrix for the model parameters of the layers below i th layer will be given less weight, however, for the i th layer and layers above i th layer will get 100 % weight for RMT. Here, d_i is the depth of the bottom of the i th layer. Similarly, weighting elements are calculated for TEM and HEM methods.
4. The data weighting matrix, \mathbf{W}_d , containing the data errors/noise is also multiplied to the elements of the Jacobian of the joint inversion matrix. To nullify the effect of the number of data points of a particular data set in joint inversion, the Jacobian is multiplied with the square root of the ratio of total number of data points in all the methods to the number of data points in the particular method.

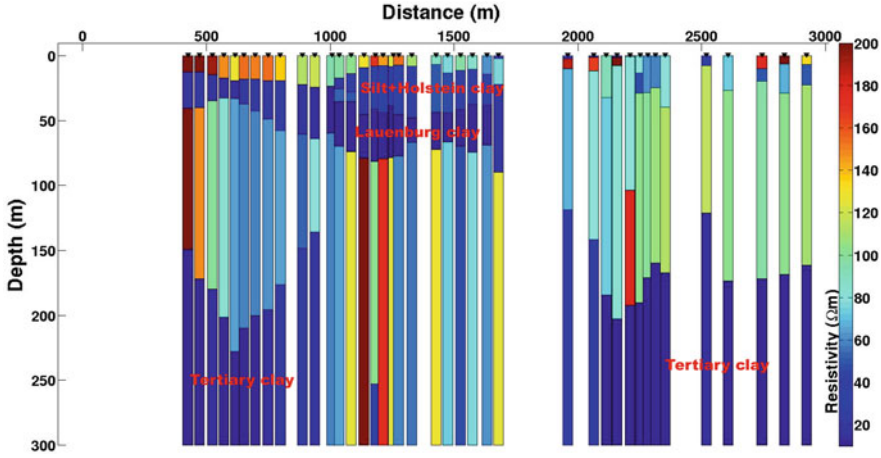


Fig. 2.4 The 1D Marquardt weighted-joint interpreted models for RMT, HEM and TEM data

5. This matrix is multiplied to the Jacobian matrix of the joint inversion and then inverted. Therefore, the resultant sensitivity matrix for weighted-joint inversion becomes

$$\mathbf{J}_w = \mathbf{W}_d \mathbf{J} \mathbf{W}_m \sqrt{\frac{\sum N}{N}}, \quad (2.2)$$

where $\sum N$ is the sum of the number of data points of all methods and N is the number of data points in a particular method.

6. The weighting matrix \mathbf{W}_m is updated after every iteration according to the new model obtained after each iteration and the inversion continues.

We used the Levenberg-Marquardt (Levenberg 1944; Marquardt 1963) inversion method, which provided damped least square solution by adding constant multiplier (β) as

$$\Delta \mathbf{m} = (\mathbf{J}_w^T \mathbf{J}_w + \beta^2 \mathbf{I})^{-1} \mathbf{J}_w^T \mathbf{y}. \quad (2.3)$$

where $\mathbf{y} = \mathbf{d} - \mathbf{f}$ is the difference between the measured data vector (\mathbf{d}) and the computed response (\mathbf{f}) at each iteration.

We have applied the weighted-joint inversion methodology on the Cuxhaven tunnel valley. Figure 2.4 illustrates the 1D Marquardt weighed-joint inversion models. The Marquardt models indicate a three to five layer geological structure. In the central part, i.e. in the valley, five layer structures have been observed, however, on the east and west side of the valley it can be explained with a four layer structure. The Marquardt weighted-joint inversion models infer the boundaries of the Holsteinian, Lauenburg clay complex and underlying fine-grained Neogene deposits. However, the base of the Paleogene is not resolved. It has been found that the results are consistently improved in all cases for the weighted-joint inversion.

2.4 Model Coupling HEM 1D+

HEM data sets are used for both geophysical and geological modelling, e.g. for groundwater or mineral exploration. As a standard procedure, the multi-frequency HEM data are inverted to resistivity-depth models using 1D inversion methods. Since the footprint of the HEM system is rather small and smooth conductivity structures are close to 1D settings, this is a valid approach. Furthermore, our “advanced 1D inversion” methods improve 1D inversion results by taking neighbouring data points and additional information from further geophysical measurements into account (Siemon et al. 2009). However, areas of higher dimensionality (anomalies) are not recovered correctly by 1D inversion procedures and require multi-dimensional modelling. Cox et al. (2012) developed a smooth 3D inversion for airborne electromagnetic data using a moving footprint technique. Accurate multi-dimensional inversion of HEM data of an entire survey, however, is still not state of the art.

Our idea is to combine 1D and 3D inversion of HEM data (Ullmann et al. 2013b). We restrict the 3D inversion to areas of strong anomalies only. The challenging task is, besides 3D inversion itself, to define those areas where 1D inversion is not able to produce acceptable resistivity models. A newly developed search algorithm (Ullmann et al. 2013a) is used to identify areas of higher dimensionality in HEM data sets. As the quantity to be measured in HEM, the secondary magnetic field, is strongly dependent on altitude variations it cannot be used directly as input for the search algorithm. Therefore, the secondary fields are transformed to apparent resistivities which are much less dependent on altitude variations. For each frequency 2D grids of the logarithmic apparent resistivities are produced using natural neighbour interpolation. The cell size is chosen of the order of a quarter of the line spacing. The search algorithm, consisting of several image processing methods, is then applied to the apparent resistivity grids. The results are added up to use all information about existing anomalies together coming from different depths, i.e. different frequencies (Fig. 2.5 left). The identified anomalies are sorted in five different classes (‘2D’, ‘3D circular’, ‘3D oval’, ‘3D elongate’, ‘chaotic’). In two steps, the region-based shape descriptors compactness, eccentricity, elongation, and deficit of convexity are grouped to the corresponding classes using the k-means algorithm. The anomalies are divided into 2D and 3D structures, in which the 3D structures are differentiated into circular, oval, or elongated shapes. The class ‘chaotic’ contains big anomalies consisting likely of overlapping single anomalies induced by different bodies in or on the subsurface (Fig. 2.5 centre). The classification results are used for optimised 3D model set-up.

A certain area containing the anomaly of interest is defined based on the result of the search algorithm (Fig. 2.5 right). In this region the HEM data have to be modelled in 3D. The corresponding HEM data are extracted for 3D inversion. Outside the anomalous region, the HEM data are inverted to resistivity-depth models using a standard 1D inversion method based on a starting model derived from apparent resistivities and centroid depth values. The anomalous HEM data are inverted to a 3D resistivity model applying a newly developed inversion scheme (Scheunert

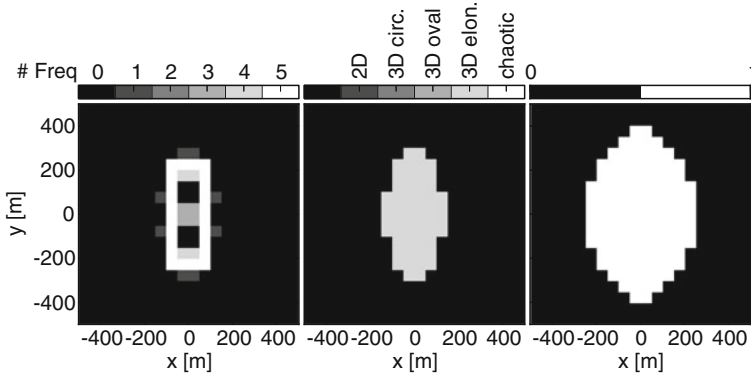


Fig. 2.5 Location and number of frequencies where anomalies were detected (*left*) and the classification scheme of detected anomalies (*centre*). Resulting anomalous region necessary for 3D inversion (*right*)

et al. 2013). The 3D inversion is carried out for a finite difference discretization using the given 1D background. Finally, the 3D inversion model (Fig. 2.6b and c) of the anomalous region can be integrated into the quasi 1D background (Fig. 2.6a). The integration of the resulting 3D models requires that the layered background coincides with the quasi 1D environment outside the anomalous region. This is generally not the case except for some small isolated structures. Therefore, the data sets have to be transformed to a 1D background (normal field transform) and, after 3D inversion, back-transformed to the originally environment. Figure 2.6d shows the resulting 1D/3D inversion model. The combination of 1D and 3D inversion of HEM data is demonstrated on synthetic HEM data derived from a 3D resistivity model (Fig. 2.7) as published by Siemon et al. (2009).

2.5 HEM 3D Inversion

Based on the precedent localisation of the entire HEM survey to those parts which are actually affected by an expected 3D anomaly (Sect. 2.4) we have developed an inversion scheme capable of revealing those anomalous conductivity structures. The approach exploits a priori information, given by a state-of-the-art laterally constrained 1D inversion. We reformulate the 3D boundary value problem of the total electric field E in terms of the secondary electric field E_{sec}

$$E = E_{\text{pri}} + E_{\text{sec}}, \quad (2.4)$$

$$\nabla \times \nabla \times E_{\text{sec}} + i\omega\mu_0\sigma E_{\text{sec}} = -i\omega\mu_0(\sigma - \sigma_{\text{pri}})E_{\text{pri}} \quad \text{in } \Omega, \quad (2.5)$$

$$n \times E_{\text{sec}} = 0 \quad \text{on } \partial\Omega, \quad (2.6)$$

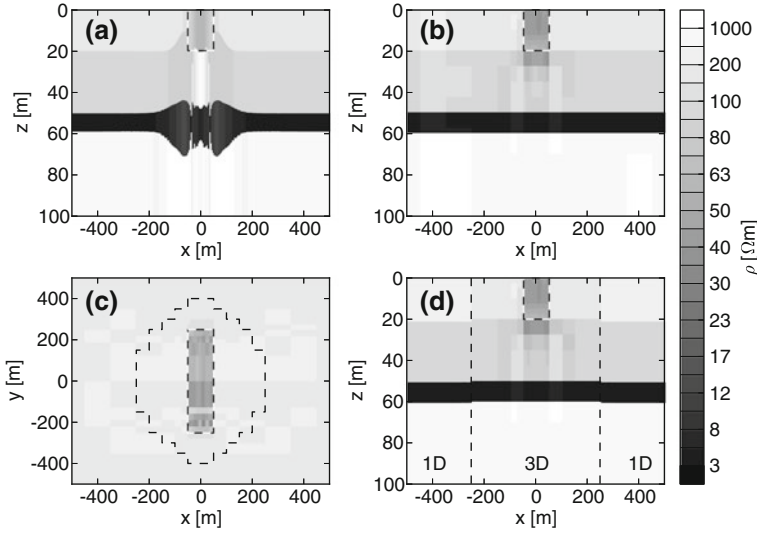


Fig. 2.6 1D (a) and 3D (b) inversion results along a profile across the model centre. *Top view* on the 3D inversion model (c) and combination of 1D and 3D inversion results (d) from a and b. The dashed black-and-white line shows the location of the cube. The dashed black line indicates the border of the previously defined area

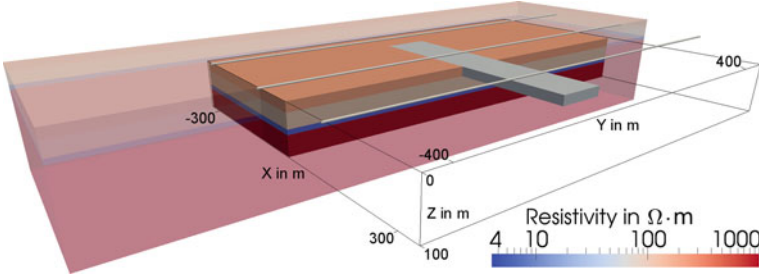


Fig. 2.7 Sketch of the model domain excluding the air layer and about half of its front-facing part. The semi-transparent part hints at the full size of the model ($1200 \text{ m} \times 1800 \text{ m} \times 350 \text{ m}$) where a rectangular block ($500 \text{ m} \times 100 \text{ m} \times 20 \text{ m}$ with $50 \Omega \cdot \text{m}$) is embedded in a horizontally layered half-space (layer depths 20 m ; 30 m ; 10 m ; 190 m with $200 \Omega \cdot \text{m}$; $100 \Omega \cdot \text{m}$; $5 \Omega \cdot \text{m}$ and $1000 \Omega \cdot \text{m}$ from top to bottom). The black outline indicates the bounds of the active region. Survey profiles are indicated by the white tubes

where E_{pri} is the analytical primary electric field of a vertical magnetic dipole located in air. Furthermore we denote by ω the angular frequency, μ_0 the vacuum permeability, σ the total conductivity, and σ_{pri} the conductivity of the background model, respectively. We employ both finite difference and finite element methods to transform the continuous boundary value problem into a system of linear equations

$$A(\sigma) u_{\text{sec}} = -A(\sigma) u_{\text{pri}} + A(\sigma_{\text{pri}}) u_{\text{pri}} = b, \quad (2.7)$$

with u_{sec} the secondary and u_{pri} the primary field solution of the discretised forward problem. The resulting system subsequently yields expressions for the gradient and approximate Hessian of the minimisation problem (sensitivity equations). Resulting from the unique transmitter-receiver coil configuration of the HEM problem, an explicit representation of the Jacobian matrix is used. To handle the sensitivity-related quantities, a tensor-based problem formulation is exploited. For solving the inverse problem, we apply a Gauss-Newton method with a Tikhonov-type regularisation term

$$\frac{1}{2} \underbrace{\|d^{\text{obs}} - d(m)\|_2^2}_{\text{data misfit}} + \frac{\lambda}{2} \underbrace{\|W(m - m_{\text{ref}})\|_2^2}_{\text{model roughness}} \rightarrow \min_m, \quad (2.8)$$

$$m := \log \sigma, \quad (2.9)$$

where we aim at finding a model parameter distribution m such that both the difference between measured data d^{obs} and predicted data from the forward solution $d(m)$ for a given model parameter set as well as the parameter roughness are minimal. For the latter we consider the action of the model weighting matrix W on the difference between the model parameter vector and a reference model m_{ref} , i.e. the known background model. The model roughness itself is weighted by the regularisation parameter λ . Therefore, the predicted data is identified by

$$d(m) = Q[A^{-1}(m)b + u_{\text{pri}}]. \quad (2.10)$$

Here Q denotes the measurement operator, capable of extracting the total fields at distinct receiver sites from the discrete field components within the computational domain. The derived linear least squares problem is solved with Krylov subspace methods, such as LSQR, that are able to deal with the inherent ill-conditioning (Hestenes and Stiefel 1952; Paige and Saunders 1982). We further include two types of implicit regularisation schemes that simultaneously reduce the amount of model parameters and the computational cost. Based on the cumulative sensitivities (footprint) for the survey setup and the background resistivity known a priori, we define an active region as part of the parameterisation of the inverse problem where changes of m are explicitly allowed. Additionally we utilise a coarse parameter grid that is the starting point for an (adaptively) refined modeling forward grid. For numerical simulations and inversion studies we used a synthetic model (Siemon et al. 2009) that is shown in Fig. 2.7. We aim at reconstructing the electrical resistivity distribution of $M = 33,600$ parameter cells of the active region. The data points are distributed over three parallel profile lines. The line spacing is 200 m. Along the profiles, data is sampled every 4 m. The height of the transmitter-receiver pair above ground is $h = 30$ m. Samples of the vertical magnetic field have been collected for five frequencies. The synthetic data set comprises $N = 3765$ data points. Figure 2.8 shows a reconstruction of the conductivity distribution obtained from an inversion

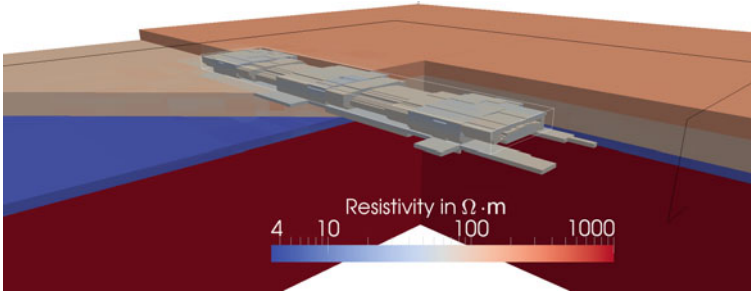


Fig. 2.8 Inversion result: Spatial distribution of the electrical resistivity. For scale and orientation refer to Fig. 2.7

of synthetic data. The final model shows an overall good agreement with the true model. After 20 Gauss-Newton iterations, the relative data residual has dropped to $1.9 \cdot 10^{-4}$. Furthermore, a smooth transition between the active and inactive region of the model is obtained due to an appropriate boundary condition imposed for the discretised model regularisation operator.

2.6 Potential Fields, Evolutionary Algorithms and Data Evaluation

In this paragraph we focus on two different tasks firstly on 3D inverse and forward modelling by evolution strategy for inversion of potential field data and secondly resampling of mass data.

We developed an interactive optimization-approach capable of combining manual modelling with automated covariance-matrix-adoption-evolution-strategy (CMA-ES, Ostermeier et al. 1994) geometry optimization. We focussed on the aspects of user-interactions supported by constrained and topology-conserving methods. In realistic geophysical models the number of geometry-describing triangles is often in the order of several hundreds of thousands. If triangles get small, the probability of incorrect and topology-destroying cross-overs increases with time. Unfortunately a destroyed topology cannot be formulated by a smooth penalty. The model is either valid or not. If it is not valid it has to be discarded. This fact leads quickly to an under-representation of good (valid) solutions, which implies that CMA-ES cannot adapt to the “landscape of the quality function” as desired. The optimization process slows down and most often stops completely. CMA-ES is strong in terms of global convergence and flexible in terms of adoption to the (local) quality function. This is achieved by learning a mutation-distribution on the fly. The method can deal with high-dimensional, highly scaled parameter spaces and fast convergence is achieved on a variety of typical test cases. But CMA-ES cannot guarantee topology-conservation of the models during optimization. There are two solutions

to the problem. (1) “re-injection”, where the strategy can actively be taught what a correct solution is or better would be: For example the parameter can be set (back) to—or short before—the constraining limit of the parameter and then be re-injected to the CMA-ES. This method is extremely computing intense and re-injection is not fully developed in terms of numerical stability. (2) Our idea to achieve topology conservation is to manipulate the space—which hosts the model—instead of the model itself (Alvers 1998). This can be achieved by a new paradigm where topology is preserved intrinsically. The basic idea is to change the size of grid elements (element legs) and make sure that (a) the legs are always greater than zero and (b) the element stays convex. The model behind must be sampled with high resolution as a prerequisite to always preserve topology. The idea is, to deform the models surrounding space. Thus, the model is optimized indirectly through its bent, entrapping space. In that way the model will be deformed while topology is intrinsically conserved. The model to be optimized is meshed with a regular grid in two dimensions, with e.g. tetrahedron grid in 3D. Then the grid (= containing space) is changed in such a way that the geometry of the model becomes optimal with respect to the quality function. Figure 2.9 illustrates the idea. Any grid modification is only performed along the edges of a grid element, which must not become zero-length (or negative) because the grid would touch (or even intersect) itself and the topology of the grid and therefore the topology of the model behind would be again destroyed. Model parameters are shifted to the length of the grid sides/legs. Now the coarse and fine grids control the possible geometry-resolution and therefore the number of optimization parameters. The beauty of this approach is that the user has full control and is not directly confronted with a highly resolved model with a huge number of triangles. In the 3D case the handles used to distort the room are defined in a cube or on tetrahedrons. The resolution of the cube can also be adjusted such that model updates can be either more focused or may affect a larger area. This is obviously useful to switch between detailed work and more regional model updates. More regional updates in the deeper parts of the model are also useful because the user gets immediate feedback on the model changes. This method is generic and can be applied to polyhedral models, voxel models and hybrid models (Schmidt et al. 2011). Inversion is typically done in batch where constraints are defined beforehand and then after a few minutes or hours a model fitting the data and constraints is generated. Quite often these models fit the data but appear to be unrealistic and the constraints are changed in order to improve the solution. Constraints can be entered directly (for example the maximum depth of an interface) or implemented indirectly (for example in the regularization). True geological constraints are difficult to implement because of their complexity.

Many data sets in geosciences contain extreme large amount of data. The high point density of these data sets often causes problems for processing and visualization. For efficient numeric handling, diverse resampling techniques are used to ease the data for better computation performance. Most common resampling methods usually reduce either highly resolved gridded data regularly or interpolate dense scattered 3D points on a coarse point grid. Because of parameter independency and interpolation, these methods cause a high loss of information. To avoid this problem, the presented “CIDRe” framework was developed (CIDRe: “Constrained Indicator

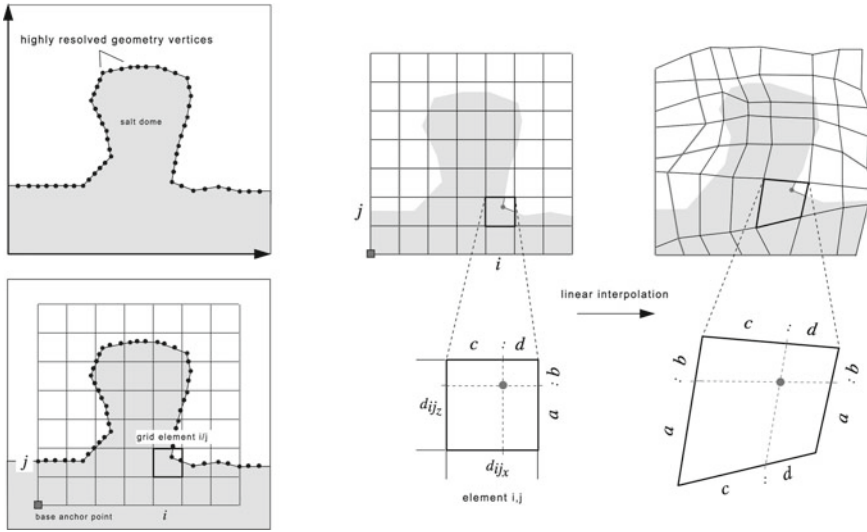


Fig. 2.9 *Left* A geological structure (salt dome) is meshed with a grid. *Right* The grid deformation is performed on grid legs and the model is interpolated linearly

Data Resampling”). The framework gets use of an irregular resampling method to improve handling, visualization and exchangeability of data and results. The new resampling algorithm uses the given data-parameters as resampling constraints (e.g. elevation, measured gravity or apparent resistivity). Accordingly the resampling chooses points, which are essentially important for the data set and rejects points with low additional information. Interpolation is not needed for resampling, so this method causes much lower errors than regular or interpolating resampling methods with similar resampling rates, in particular for data with strongly varying parameter distributions.

To demonstrate the achieved resampling results, the “CIDRe”—framework was applied on real HEM data (Siemon et al. 2004), that were used for inversion of observations in Sects. 2.3–2.5 and as constraints for geological modelling in Sect. 2.7. The resampling result is shown in Fig. 2.10, the parameter “apparent resistivity” ρ_a , inverted for the secondary field measured with a frequency of 385 Hz, was chosen as resampling constrain.

2.7 Model Development and Evaluation

One of the primary goals was the integration and assimilation of the results of the AIDA project partners in the framework of its examinations of plausibility and visualization of modelling and inversion. Here we will provide a priori conditions for structural model design as it results from 1D and 3D HEM-inversion.

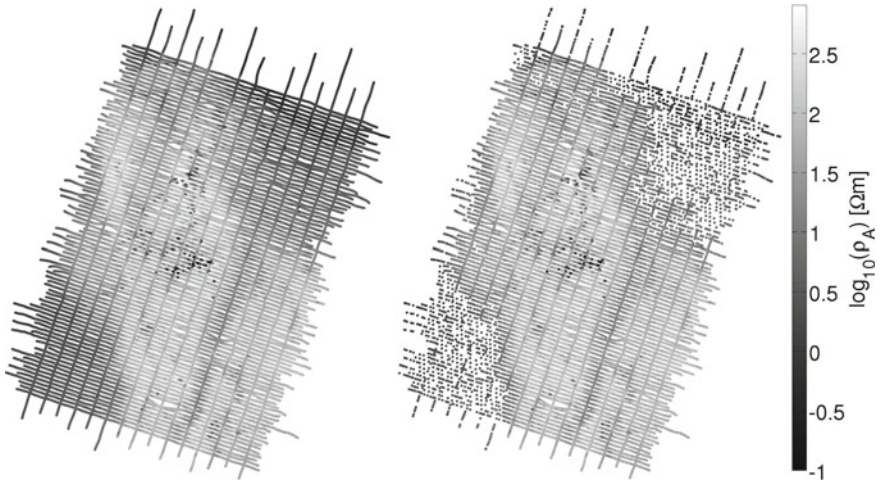


Fig. 2.10 Original (*left*) and resampled (*right*) ρ_a data. The resampling result achieves an average difference of 0.19 % to original parameter distribution for a resampling rate of 22.3 %

The aim of the joint project is an improved user oriented interpretation of combined 3D inversion and modelling of near subsurface data derived from airborne and ground-based geophysics. This was achieved by the development of an integrated workflow and new 3D modelling approaches, based on the integration of different geophysical, sedimentological, and petrophysical data. The main task was to combine geophysical and geological data sets to provide more realistic 3D subsurface models. In general, the ambiguity of geological, hydrogeological and geophysical data can lead to uncertainties in the resulting subsurface models. These uncertainties are caused by (1) limited data coverage (boreholes, seismic profiles, electromagnetic); (2) the limited vertical and lateral resolution of airborne electromagnetics (HEM and SkyTEM) and (3) the correlation of geophysical and lithological/hydrogeological properties (e.g. Burschil et al. 2012; Klimke et al. 2013). The workflow in Fig. 2.11 was established to reduce these uncertainties: First, pre-existing geophysical and geological data sets were used to build independent 3D subsurface models. The geological 3D subsurface models were constructed based on borehole data and 2D seismic reflection profiles. In a next step, the 1D AEM inversion results were utilized to construct a 3D resistivity grid model of the subsurface. To achieve this, we constructed a regular spaced grid and integrated the 1D AEM inversion results and subsequently analyzed the data by means of geostatistical methods such as nearest neighbour, discrete smooth interpolation algorithm and kriging. The best results were achieved by kriging. The advantage of this procedure is that it provides a fast selection of three-dimensional objects with specific resistivity ranges and therefore provides a rough estimate about the depositional architecture. To test the accuracy of the 3D resistivity model we calibrated it with seismic facies and lithological logs. The general correlation of grain size classes and resistivity values allows for a rough

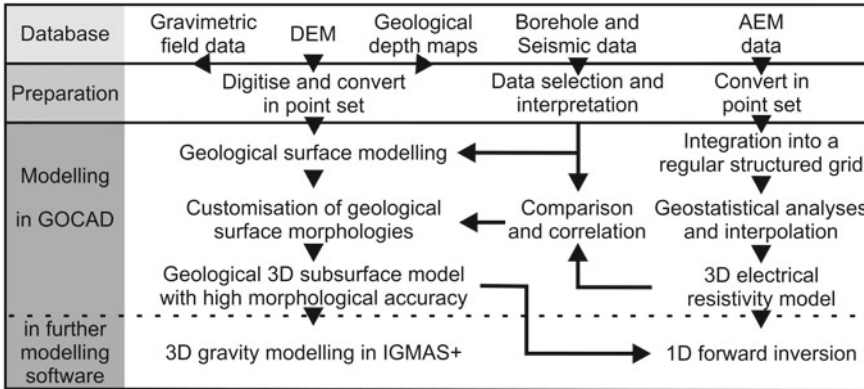


Fig. 2.11 Workflow for geological evaluation of geophysical models from different subprojects of the AIDA research partners

correlation of airborne electromagnetic data and lithology. However, the effect of overlapping resistivity values with different grain size classes may result in a misinterpretation of the lithology. The correlation between seismic facies, reflector patterns and AEM data enables the reconstruction of larger scale architectural elements and bounding surfaces. Resistivity images probably also allow the detection of fracture and fault systems. Open fractures may act as fluid conduits and therefore are characterized by a higher water content and hence a resistivity pattern that differs from the surrounding rocks. Subsequently, the 3D resistivity model and the 3D subsurface model were integrated and the initial parameters and boundary conditions of the geological model were adjusted. In the final step, 3D subsurface models were validated by comparing AEM forward modelling results based on these geological models with measured AEM results to identify remaining uncertainties. Additionally the models were used as input for 3D gravity modelling in IGMAS+. Therefore interfaces between IGMAS+ and GOCAD® and/or other user software in the AIDA project has to be developed and implemented.

An interface infrastructure was implemented for data exchange, processing and visualization to support the integration of particular results. This improvement consists of separate scripts, tools and applications and additionally integrates the “CIDRe”-framework, which was already introduced in Sect. 2.6. For purposes documented below, interfaces for TSurf-data (GOCAD®) and IGMAS+ XML-data were provided. The 3D geological model geometry for the Cuxhaven tunnel valley (Sect. 2.2) will be validated later by the synthetic gravity effect, calculated by gravity forward modelling.

Closed polyhedral subsurface geometries were extracted as TSurf-objects. These geometries were represented by triangulated hulls for each stratigraphic unit, which can be imported to the gravity forward modelling software IGMAS+ (Schmidt et al. 2011). Topographic geometry parts with elevation above 0 m are removed.

Additionally, model boundaries are extended by 15-fold model extension in each direction to avoid computational edge effects.

In IGMAS+ for each triangulated body hull a “body” object is assigned to this geometry to encapsulate the geophysical subsurface parameters, e.g. density. The parameter set is assumed to be constant for the entire body geometry. Earlier studies already showed that the gravity signal of the infilled masses of a tunnel valley varies between $-0.3 * 10^{-5} \frac{m}{s^2}$ (Rumpel et al. 2009) and $0.3 * 10^{-5} \frac{m}{s^2}$ (Gabriel et al. 2003). The anomalies depend on the different densities of the infill. Stronger anomaly differences in mentioned studies are associated with the density values of the parametrization of the “Lauenburg Clay Complex (LCC)” (Rumpel et al. 2009). It varies between densities of $1813 \frac{kg}{m^3}$ and $1996 \frac{kg}{m^3}$ (Gabriel et al. 2003). From this we concluded, that the negative gravity anomaly interpreted by Rumpel et al. (2009) is mainly associated with rather low LCC densities. Generally we are in agreement with Rumpel et al. (2009) and Gabriel et al. (2003) that the tunnel valley fill is characterized by higher densities than the surrounding Neogene host sediments. Therefore, the gravity effect of the Lauenburg Clay Complex may mask the gravity anomalies of the basal coarse-grained tunnel valley fill.

According to these results, the geological architecture can be regarded as plausible. The LCCs density remains rather uncertain: gravity forward modelling suggests a density value of some $1900 \pm 20 \frac{kg}{m^3}$ for the LCC.

2.8 Discussion of Results

The AIDA results demonstrate that combined 3D geological and geophysical models enable a much better reconstruction of the subsurface architecture. The combination of an unmanned aerial system (UAS) with the very low frequency (VLF) method was successfully tested. Areas with low data coverage can be interpolated based on AEM data, if the correlation of resistivity values and lithology is known. In general the penetration depth is controlled by the lithology and their conductivity. SkyTEM data have a higher penetration depth (up to 300 m) but a lower vertical and lateral resolution, restricting the visualization of smaller-scale geological features. In contrast, the HEM method provides a much higher vertical and lateral resolution, but a lower depth penetration of up to 150 m.

New methods were developed and tested for the interpretation of AEM data, which mainly based on 3D modelling approaches. (1) In particular we used 1D AEM inversion results and applied a new 3D resistivity gridding procedure based on geo-statistical analyses and interpolation techniques to create continuous 3D resistivity grid models. This integrated workflow minimizes uncertainties in the interpretation of AEM data and allows for a significantly improved interpretation and imaging of the 3D subsurface. (2) The limits in the lateral and vertical resolution may lead to a diffuse reconstruction of thin-bedded sand/mud couplets, smaller-scale architectural elements and bounding surfaces, shown by Jørgensen et al. (2003), Viezzoli et al. (2008), Christensen et al. (2009) and Klimke et al. (2013). (3) The effect of

overlapping resistivity values with different grain size classes, as well as the effect of salt or fresh Water in saturated sediments may result in a misinterpretation of the lithology (Burschil et al. 2012; Klimke et al. 2013). (4) Anthropogenic noise effects in the AEM data can hinder a proper geological interpretation. Several new studies focus on the determination and elimination of these noise effects and their minimization (e.g. Tølbøll 2007; Siemon et al. 2011).

In order to enhance the model accuracy airborne and ground-based measurements (e.g. HEM, RMT and TEM) can be combined by joint inversion.

Automatic detection and handling of conductivity anomalies for in- and output routines were developed and tested; they enable to restrict 3D modelling only into areas where 3D modelling is really necessary. In all other cases a 1D inversion scheme is suggested. The user interface HEM1D+ controls all modelling interactions.

Inversion is typically done in batch where constraints are defined beforehand and then after a few minutes or hours a model fit of data and constraints is generated. Quite often these models fit the data but appear to be unrealistic and the constraints are changed in order to improve the solution. Constraints can be entered directly (for example the maximum depth of an interface) or implemented indirectly (for example in the regularization). True geological constraints are difficult to implement because of their complexity.

We developed a new novel weighted 1D weighted-joint inversion algorithm for the TEM, RMT and HEM data which was first of all tested by synthetic data and was then applied on a field data set. The weighted-joint Marquardt inversion models clearly infer the boundaries of the Lauenburg and Holsteinian clay complex in the common test area. To recover the spatial distribution of electrical conductivities from HEM data sets a 3D inversion scheme was developed, implemented and successfully applied. The inverse problem is solved using a Gauss-Newton approach. A novel method to evaluate and store the Jacobian leads to a noticeable reduction of computational effort. Together with state-of-the-art regularization techniques, the improved efficiency yields a substantial progress in the field of EM inversion methods. Based on the precedent localization of the entire HEM survey to those parts which are actually affected by an expected 3D anomaly we have developed an inversion scheme capable of revealing those anomalous conductivity structures. The approach exploits a priori information, given by a state-of-the-art laterally constrained 1D inversion.

A new scheme of inversion was developed during the runtime of the project. It is integrated in the interactive workflow to support typical trial and error approaches. Instead of alter a geological interface manually the user can kick off a (topology-conserving) inversion in a focused area, watch the inversion progress on the screen and interrupt in case the solution becomes geologically unrealistic. One can then wind a few steps back, change parameters of the inversion (e.g. change the selected region or change constraints) and start over. Thus the user always stays in control of the inversion process.

Problems arise from the spatial consistency of different geometries used in different software. They concern the geometrical GOCAD[®] and density modelling software (IGMAS+): triangulated hulls for each subsurface region have to be consistently closed, which means that each triangle edge of the hull mesh has to be shared

by two triangles in an opposite direction. This requirement is needed for correct gravity calculation in IGMAS+ (Schmidt et al. 2011) but not for GOCAD®. Therefore, each GOCAD-mesh has to be checked for geometrical consistency before it can be inserted in IGMAS+ for forward modelling. Further limitations are related to material parameters. The stratigraphic units can be detected by apparent resistivities and not always by densities. Toward this end the given geometry of the geological model does not represent subsurface densities. However, we demonstrated that the geological model cause a gravity field which fits published data.

2.9 Conclusions and Future Tasks

We provide fast and accurate methods for integrated 3D models of the subsurface both for geometry and parameters by resistivity grid modelling by the interpolation of 1D AEM inversion data and 3D forward modelling of terrestrial (gravity) data. The comparison of our integrated models with 1D AEM inversion results (Sect. 2.7) shows a significant improvement of the interpretation of AEM data and thus an improved reconstruction of the 3D subsurface architecture. AIDA project partners mostly achieved the primarily addressed goals. The handling of 3D models is restricted to models which were calculated (a) by forward modelling techniques and (b) inverted models based on synthetic data. Intensive collaboration within the AIDA project focussed on subprojects which directly got use of HEM, TEM and RMT data e.g. in the test area of Cuxhaven tunnel valley by both 1D inversion results and in-output interfaces of synthetic HEM data and/or models. As a result, a workflow was developed which recovers a 3D conductivity structure from subsets of large HEM data sets. These subsets have been reliably identified by research described in Sect. 2.4 on the basis of an anomaly detection algorithm. The 3D conductivity models obtained by the application of a 3D inversion (refer to Sect. 2.5) which have later been successfully merged with the original model based on local 1D inversions. The integration of borehole, seismic and AEM data into a Gocad model led to highly accurate geological 3D subsurface models at both test sites and proved the consistency of electrical resistivity models. A combination with density modelling was much more difficult because reliable information for both Bouguer gravity field and densities are still missing in the area of the Cuxhaven tunnel valley. The geological model did not really fit the measured gravity field. More generally we conclude from the intensive disciplinary collaboration that interactive geophysical modelling is tedious and very complex. Automated methods must at least support the experts and the connected problems are severe. The usage of automated optimization methods is problematic in case many solutions need to be rejected because of the model becoming inconsistent. However, the combined strategy of interactive optimization and space warping, instead of moving the corner points of the geometry directly, eased this problem.

We developed and suggest a couple of new inversion schemes, which are integrated in the interactive workflow to support geological interpretation. However, uncertainties in the integrated interpretation of AEM and ground data remain, mainly caused

by limitation related to their lateral and vertical resolution, anthropogenic noise effects, effects of overlapping resistivity values with varying grain size classes and pore water characteristics. Future work should focus on the determination and elimination of these uncertainties and their minimization. We will emphasize the need for highly-developed numerical regularization techniques such as the total variation regularization which employ jump-preserving features that might be necessary when appropriate geological a priori data is available. However, in conventional inversion procedures, constraining boundary conditions are assigned to “points” and topologically incorrect models are rejected. This often leads to problems like “extinction” of good individuals/solutions due to rather “small errors”. Human experts can often—but not always—keep topology through their knowledge about possible geological structures and their developments. To teach this to algorithms is impossible. Artificial neural networks (e.g. Gunnink et al. 2012) and sequential indicator simulations (e.g. Bosch et al. 2009) might be interesting in future to distinguish between different lithologies, parameter contrasts and depositional architecture of the subsurface. The developed algorithms still need more optimization towards intensive tests with real world data.

Acknowledgments The AIDA-Verbundprojekt is part of the support program GEOTECHNOLOGIEN of the BMBF: “Tomography of the Earth’s Crust—From Geophysical Sounding to Real-Time Monitoring”. We appreciate the financial support of our project by the BMBF and its administration by the Projektträger Jülich.

References

- Alvers MR (1998) Zur Anwendung von Optimierungsstrategien auf Potentialfeldmodelle. PhD thesis, FU Berlin (SFB 267), Berliner Geowissenschaftliche Abhandlungen, Reihe B, Band 28, Berlin, 108 Seiten.
- Bosch JHA, Bakker MAJ, Gunnink JL, Paap BF (2009) Airborne electromagnetic measurements as basis for a 3D geological model of an Elsterian incision. *Zeitschrift der deutschen Gesellschaft für Geowissenschaften* 160(3):249–258
- Burschil T, Scheer W, Kirsch R, Wiederhold H (2012) Compiling geophysical and geological information into a 3D model of the glacially-affected island of Föhr. *Hydrol Earth Syst Sci* 16:3485–3498
- Christensen NB, Reid JE, Halkjær M (2009) Fast, laterally smooth inversion of airborne time-domain electromagnetic data. *Near Surf Geophys* 7:599–612
- Cox LH, Wilson GA, Zhdanov MS (2012) 3D inversion of airborne electromagnetic data. *Geophysics* 77(4):WB59–WB69
- Eröss RB, Stoll JB, Tezkan B (2013) Three-component VLF using an unmanned aerial system as sensor platform. *First Break* 31(7):33–41
- Gabriel G, Kirsch R, Siemon B, Wiederhold H (2003) Geophysical investigation of buried Pleistocene subglacial valleys in Northern Germany. *J Appl Geophys* 53:159–180
- Gunnink JL, Bosch JHA, Siemon B, Roth B, Auker E (2012) Combining ground-based and airborne EM through artificial neural networks for modelling hydrogeological units under saline groundwater conditions. *Hydrol Earth Syst Sci* 16:3061–3074
- Hestenes RM, Stiefel E (1952) Methods of conjugate gradients for solving linear systems. *J Res Nat Bur Stan* 49(6):409–436

- Jørgensen F, Lykke-Anderson H, Sanderson PBE, Auken E, Nørmark E (2003) Geophysical investigations of buried Quaternary valleys in Denmark: an integrated application of transient electromagnetic soundings, reflection seismic surveys and exploratory drillings. *J Appl Geophys* 53:215–228
- Klimke J, Wiederhold H, Winsemann J, Ertl G, Elbracht J (2013) Three-dimensional mapping of Quaternary sediments improved by airborne electromagnetics in the case of the Quakenbrück Basin, Northern Germany. *Zeitschrift der deutschen Gesellschaft für Geowissenschaften* 164(2):369–384
- Levenberg K (1944) A method for the solution of certain non-linear problems in least squares. *Q Appl Math* 2:164–168
- Littke R, Bayer U, Gajewski G, Nelskamp S (2008) Dynamics of complex intracontinental basins. The example of the Central European Basin System. Springer, Heidelberg, p 519
- Marquardt DW (1963) An algorithm for least-squares estimation of non-linear parameters. *SIAM J Appl Math* 11:431–441
- Ostermeier A, Gawelezyk A, Hansen N (1994) A derandomized approach to self-adaptation of evolution, strategies. *Evol Comput* 2(4):369–380
- Paige CC, Saunders MA (1982) LSQR: an algorithm for sparse linear equations and sparse least squares. *ACM Trans Math Softw* 8(1):43–71
- Rumpel HM, Binot F, Gabriel G, Siemon B, Steuer A, Wiederhold H (2009) The benefit of geophysical data for hydrological 3D modelling—an example using the Cuxhaven buried valley. *Zeitung der deutschen Gesellschaft für Geowissenschaften* 160(3):259–269
- Scheunert M, Afanasjew M, Börner RU, Einermann M, Ernst OG, Spitzer K (2013) 3D inversion of helicopter electromagnetic data. In: 5th international symposium on three-dimensional electromagnetics, Sapporo, Japan, Extended Abstract, p 4
- Schmidt S, Plonka C, Götze HJ, Lahmeyer B (2011) Hybrid modelling of gravity, gravity gradients and magnetic fields. *Geophys Prospect* 59(6):1046–1051
- Siemon B, Eberle DG, Binot F (2004) Helicopter-borne electromagnetic investigation of coastal aquifers in north-west germany. *Zeitschrift für Geologische Wissenschaften* 32(5/6):385–395
- Siemon B, Auken E, Christiansen AV (2009) Laterally constrained inversion of helicopter-borne frequency-domain electromagnetic data. *J Appl Geophys* 67(3):259–268
- Siemon B, Steuer A, Ullmann A, Vasterling M, Voß W (2011) Application of frequency-domain helicopter-borne electromagnetics for groundwater exploration in urban areas. *Phys Chem Earth, Parts A/B/C* 36(16):1373–1385
- Spies BR (1989) Depth of investigation in electromagnetic sounding methods. *Geophysics* 54:872–888
- Tølbøll RJ (2007) The application of frequency-domain helicopter-borne electromagnetic methods to hydrogeological investigations in Denmark. PhD thesis, Department of Earth Sciences, University of Aarhus, Denmark
- Ullmann A, Siemon B, Miensopust M (2013a) Automatic detection and classification of induction anomalies in helicopter-borne electromagnetic data sets. In: 5th international symposium on three-dimensional electromagnetics, Sapporo, Japan, Extended Abstract, p 4
- Ullmann A, Siemon B, Scheunert M, Afanasjew M, Börner RU, Spitzer K, Miensopust M, (2013b) Combined 1D and 3D inversion of helicopter-borne electromagnetic data. In: Near surface geoscience, (2013) Bochum, Extended Abstract, Germany, p 5
- Viezzioli A, Christiansen AV, Sørensen K (2008) Quasi-3D modelling of airborne TEM data by spatially constrained inversion. *Geophysics* 73(3):F105–F113

Tomography of the Earth's Crust: From Geophysical
Sounding to Real-Time Monitoring

GEOTECHNOLOGIEN Science Report No. 21

Weber, M.; Münch, U. (Eds.)

2014, X, 176 p. 84 illus., 28 illus. in color., Hardcover

ISBN: 978-3-319-04204-6